Available online at www.sciencedirect.com
ScienceDirect
Acta Materialia 59 (2011) 640–650
Acta MATERIALIA
www.elsevier.com/locate/actamat

Structure and mechanical properties of Ti–6Al–4V with a replicated network of elongated pores

Daniel J. Jorgensen [1], David C. Dunand *

Department of Materials Science and Engineering, Northwestern University, Evanston, IL 60208, USA

Received 12 January 2010; received in revised form 21 June 2010; accepted 19 September 2010
Available online 26 October 2010

Abstract

Ti–6Al–4V, with a network of elongated, open pores aligned along two perpendicular directions, is produced by a two-step replication process: (i) Ti–6Al–4V powder or foil preforms containing low-carbon steel wire meshes are densified by hot pressing under transformation superplasticity conditions; (ii) porosity is created by electrochemical dissolution of the low-carbon steel wires and the adjacent Fe-containing Ti–6Al–4V matrix. If high-carbon steel wires are used, Fe diffusion into Ti–6Al–4V is inhibited by a carbide layer forming at the wire/matrix interface, and pores exactly replicate the shape of the wires. Ti–6Al–4V with ~19% and 34% porosity, without and with Fe–Ti interdiffusion respectively, shows low oxygen contamination and good compressive ductility. Strength and stiffness, as measured by compression testing and ultrasonic measurements, are compared with simple analytical models and numerical finite-element models.

Keywords: Porous material; Titanium alloys; Powder processing; Superplasticity; Space-holder electro-dissolution

1. Introduction

Commercially pure titanium (CP-Ti) and the titanium alloy Ti–6Al–4V are extensively used as implants in the medical industry because of their surface oxide biocompatibility, corrosion resistance, high strength and low density [1]. Furthermore, the low stiffness of titanium alloys as compared to the commonly used stainless steel and cobalt–chromium alloys reduces stress shielding, where low stiffness bone resorbs because the much stiffer implant carries the majority of the load [2]. Non-porous implants may also slip out due to the lack of physical anchoring mechanism, and must rely on polymer adhesives that are prone to damage and creep at body temperature [3].

While implant anchorage can be achieved with bone ingrowth into a thin porous surface layer with 200–500 μm pores [4], fully porous implants exhibit lower stiffness addressing the stress-shielding issue as well. Most processing methods for fully porous titanium are based on powder metallurgy, because of the reactivity and high affinity of molten titanium for oxygen and the detrimental effect of oxygen on titanium ductility. Existing methods for producing porous titanium are reviewed in Ref. [5] and include partial sintering of powders [6,7] or fibers [8], sintering of hollow powders [9], creep expansion of gas-filled pores [10–13], sintering around a fugitive spaceholder [14–18], direct laser/electron beam fabrication [19–23], electro-discharge sintering [24–27] and gel casting [28,29].

Creating elongated pores in titanium implants is of interest, because elongated pores more closely mimic the anisotropic bone porous architecture and can reduce stiffness (and thus stress shielding) more efficiently than equiaxed pores. Beside rapid prototyping approaches which permit the creation of titanium scaffolds with directional struts [22,23,30,31], four main powder-metallurgy processes exist to produce elongated pores in titanium. First, bundles of wires are densified in the presence of argon, which is then expanded into elongated pores by creep of the surrounding titanium matrix [11]. In a second process,

* Corresponding author. Tel.: +1 847 491 5370.
E-mail address: dunand@northwestern.edu (D.C. Dunand).
[1] Present address: Boston Scientific CRM, Arden Hills, MN 55112, USA.

1359-6454/$36.00
doi:10.1016/j.actamat.2010.09.069

powder preforms of titanium and deformable spaceholder are extruded, and the elongated spaceholder phase is later removed to produce elongated pores [32,33]. The third process involves freeze-drying a directionally solidified placeholder titanium powder slurry to leave pores that were previously occupied by elongated dendrites of water ice [34–36] or camphene [37]. The fourth process relies on the densification of titanium powder preforms containing steel wires which are subsequently electrochemically removed, as recently demonstrated for CP-Ti [38] and Ti–6Al–4V [39].

In the latter study [39], preforms of Ti–6Al–4V powders containing parallel layers of steel wire meshes were vacuum sintered for 24 h at 1050 °C, leaving 13 ± 3% microporosity in the Ti–6Al–4V matrix due to incomplete sintering. For bone implants, this equiaxed microporosity is undesirable, as it weakens the material without being accessible to bone ingrowth because of its small size. Increasing the sintering temperature to the 1200–1350 °C range needed to achieve full densification of Ti–6Al–4V is impossible, because of the presence of a Fe–Ti eutectic at 1085 °C. In the present paper, we use external pressure and induce transformation superplasticity by thermal cycling to fully densify the Ti–6Al–4V powders around the steel wire meshes, prior to electrochemical removal to create elongated pores. We also demonstrate that Ti–6Al–4V foils can be used instead of powders to create fully dense Ti–6Al–4V/steel composites and, after dissolution, porous Ti–6Al–4V. We measure compressive mechanical properties of these two types of porous Ti–6Al–4V materials (powders or foil precursors) with two levels of porosities (∼19% and ∼34%) and we compare strength and stiffness values with predictions from analytical and finite-element models.

2. Experimental procedures

2.1. Composite densification

Irregularly shaped Ti–6Al–4V powders (with 44–149 μm size range and 0.19 wt.% oxygen, produced by the hydride–dehydride process by StarMet Corp.) were used in the as-received state. Their size were larger than, and their oxygen content was similar to, the powders used in our previous investigation (44–53 μm and 0.17 wt.% O) [39]. Ti–6Al–4V foils with 800 μm thickness were purchased from McMaster-Carr (Elmhurst, IL) and cut by water jet into 19.1 mm diameter disks. Steel meshes consisted of 356 μm diameter low-carbon steel wires woven in an orthogonal pattern with wire center-to-center spacing of 1068 μm in each direction and an open area of 44%. These meshes were identical to those used in our previous study [39] and were used as received (0.13 wt.% C) or were carburized in a graphite pack in air at 960 °C for 1 h to achieve a carbon content of 0.67 wt.% C, as measured by Wah Chang Analytical Laboratory Services (Albany, OR). When steel with >0.2 wt.% carbon is in contact with CP-Ti at high temperatures, a thin, continuous TiC layer forms which inhibits the Fe–Ti interdiffusion occurring at lower carbon content [40]. Thus, the as-received and carburized meshes result in high interdiffusion and low interdiffusion, respectively, between the wires and the matrix. In the former case, the Fe-containing Ti–6Al–4V region surrounding the wires is removed electrochemically together with the steel wire, thus increasing the porosity beyond the fraction of steel wires [38,39].

Four types of samples were fabricated: (i) powder based, high interdiffusion (PHI), with Ti–6Al–4V powders and uncarburized steel mesh; (ii) powder based, low interdiffusion (PLI), with Ti–6Al–4V powders and carburized steel mesh; (iii) foil based, high interdiffusion (FHI), with Ti–6Al–4V foil and uncarburized steel mesh; and (iv) foil based, low interdiffusion (FLI), with Ti–6Al–4V foil and carburized steel mesh.

Powder-based samples were assembled in a 12.7 mm inside diameter graphite die by pouring 0.5 g powder layers (hand-compacted for flatness) interspersed with steel meshes with 8 × 8 cells whose wires were aligned to (no rotation), and formed parallel planes with, each other. Foil-based samples were created in a 19.1 mm inside diameter graphite die by laying 19.1 mm diameter disks of Ti–6Al–4V foil in alternating layers with aligned, parallel steel meshes with 12 × 12 cells. For each sample, 11 layers of matrix (powder or foil) material and 10 layers of steel mesh were used. Densification was carried according to the same procedures for both types of matrix material as follows.

The hot press was evacuated to a residual vacuum of 5×10^{-5} torr and heated to 860 °C. Once this temperature was reached, a 10 MPa uniaxial compressive stress was applied to the pistons and the temperature was cycled for 2 h between 860 and 1020 °C with near-linear heating and cooling ramps of ∼1.5 min each, to induce transformation superplasticity in the Ti–6Al–4V powders [41,42] and thus increase the powder densification rates [43–45]. A displacement transducer monitored piston displacement resulting from sample densification during thermal cycling. After 2 h, piston displacement was negligible, indicating that the sample was fully dense. Depending on the diameter of the die used (12.7 or 19.1 mm), one or two parallelepiped 4.5 × 4.5 × 9 mm samples were cut by electro-discharge machining from the densified composite. The 9 mm height (3-direction) was parallel to the applied stress and thus perpendicular to the wire mesh plane, while the two shorter 1- and 2-dimensions were perpendicular (respectively parallel) to the wires in the meshes.

After cutting, the high-interdiffusion PHI and FHI samples were annealed at 1050 °C for 6 h to increase interdiffusion between the wire and the matrix, and thus increase porosity after electrochemical dissolution.

2.2. Steel dissolution

To remove the steel wires from the Ti–6Al–4V matrix, each of the parallelepiped samples with steel exposed to the surface was first attached to a CP-Ti strip with nylon

wire to maintain electrical contact. The sample was then immersed in a 0.34 M aqueous sodium chloride solution. Acetic acid, used to accelerate dissolution process in Ref. [38], was not used here as it pitted the surface of the Ti–6Al–4V matrix [39]. The cathode was a 500 μm thick sheet of CP-Ti wrapped around the inside circumference of the 84 mm diameter beaker to produce a symmetrical radial electric field. The sample, acting as the anode, and the Ti sheet cathode were then connected to a Kaito model HY3003D DC power supply and immersed in the electrolyte. Sonication was used to remove the loosely adherent iron oxide layer formed by the electrochemical reaction and bring fresh solution to the reaction surface. A voltage of 2.5 V was found to be optimal for steel wire removal [39]: higher values overcame the natural passivation layer of the Ti–6Al–4V and oxidized both matrix and wires concurrently, while lower values reduced the kinetics of dissolution. Steel removal was verified by holding samples on a microbalance and suspending a magnet above them. After complete steel removal, Archimedes density measurements, with open porosity plugged with vacuum grease, were performed to determine the total porosity.

2.3. Mechanical testing

The times of flight of ultrasonic sound waves transmitted through the three main directions of the porous samples (with 9 mm height and $4.5 \times 4.5\ mm^2$ cross-section) were measured with two 5 MHz transducers, with molasses as the coupling material between transducers and sample. Due to the sample shape and pore orientation, orthorhombic symmetry was assumed for the stiffness tensor, which requires nine independent elastic constants, i.e. one longitudinal and two shear wave velocities for each of the three principal directions of the sample. Longitudinal wave speeds were used to calculate the axial components of the elastic stiffness matrix, C_{11}, C_{22} and C_{33}, as [46]:

$$C_{ii} = \rho v_{ii}^2 \tag{1}$$

where ρ is the sample density and v is the sound velocity. The first subscript denotes the propagation direction, while the second subscript denotes the polarization direction. For these parallelepiped samples, the 3-direction is the long direction. Shear wave measurements were used to calculate C_{44}, C_{55} and C_{66} as [46]:

$$C_{44} = \rho v_{23}^2 \tag{2a}$$

$$C_{55} = \rho v_{13}^2 \tag{2b}$$

$$C_{66} = \rho v_{12}^2 \tag{2c}$$

Because off-diagonal elastic constants were not measured (as this would have required samples cut in non-axial directions [47]), the only non-zero off-diagonal components of the stiffness matrix are assumed to be [48]:

$$C_{12} = C_{11} - 2C_{66} \tag{3}$$

with $C_{23} = C_{13} = C_{12}$, as in Ref. [48]. The elastic stiffness matrix was inverted to determine the elastic compliance matrix, S_{ij}, which was then used to calculate the Young's moduli in the three principle directions, i.e. the two transverse moduli E_{11} and E_{22}, and the axial modulus E_{33}. Standard propagation of error was used to calculate the error associated with each stiffness, compliance and Young's modulus value [49].

Uniaxial compressive testing was performed at a deformation rate of 0.1 mm s^{-1}, using crosshead displacement to determine strain after taking into account machine stiffness through prior calibration with aluminum samples. Friction was minimized by using highly fully dense polished ceramic spacers on the upper and lower faces of the unlubricated specimens. Each porous Ti–6Al–4V sample was loaded and unloaded three times along the elastic portion of the stress–strain curve before being loaded to failure. Failure occurred by shear along a plane forming an ~45° angle with respect to the loading direction and corresponding to the plane of maximum shear stress. Stress–strain curves were analyzed for elastic modulus, 0.2% yield strength and peak strength.

3. Results and discussion

3.1. Densification process

Hot-pressing with thermal cycling, which enhances Ti–6Al–4V powder densification by transformation mismatch plasticity [43–45], led to complete elimination of porosity in the Ti–6Al–4V matrix for samples produced from powders (PLI, Fig. 1b) or from foils (FLI, Fig. 1c). This is in sharp contrast to similar samples produced by pressureless sintering of Ti–6Al–4V powders for 24 h at 1050 °C, which exhibited a matrix microporosity of ~13% [39], as illustrated in Fig. 1a.

It is known that a thin, continuous TiC layer (titanium carbide is a biocompatible material [50]) forms at high temperatures at the interface between steel with >0.2 wt.% carbon and CP-Ti, and inhibits Fe–Ti interdiffusion [38,40]. Conversely, steel with <0.2 wt.% carbon content does not form a TiC layer, so iron can diffuse into the titanium matrix at 800–1000 °C [38,40]. These findings were confirmed for partially densified Ti–6Al–4V [39] and are further confirmed here for fully densified Ti–6Al–4V (Fig. 2). This figure shows that Fe in low-carbon steel wires diffused into the Ti–6Al–4V matrix over distances exceeding 200 μm, and produced two thin layers of intermetallics: $TiFe_2$ immediately adjacent to the steel wire and TiFe adjacent to the matrix (Fig. 3). By contrast, the high-carbon steel wires produced a continuous TiC layer at their interface (Fig. 3, insert), fully inhibiting interdiffusion between the steel wires and the Ti–6Al–4V matrix. These results are confirmed by etched cross-sections in Fig. 4a and c. Fig. 4a shows the PLI sample with no visible interdiffusion zone in the Ti–6Al–4V matrix surrounding the high-carbon steel wire. By contrast, Fig. 4c shows, for the PHI sample, an interdiffusion zone extending to a diameter of ~510 μm

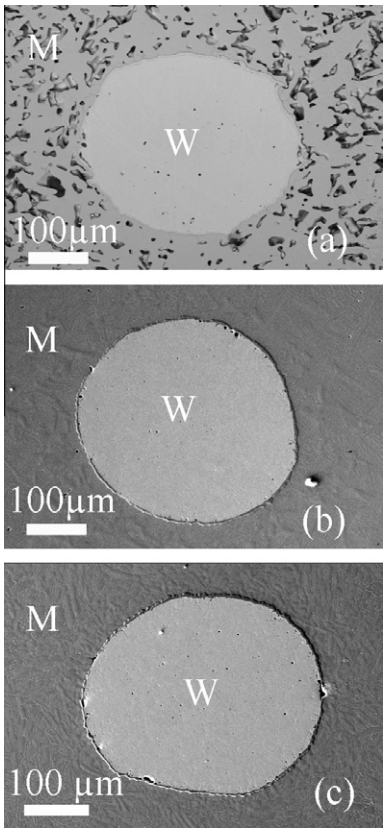

Fig. 1. Optical micrographs of cross-sections of (a) sample II from Ref. [39] sintered from powders; (b) sample PLI hot-pressed from powders; and (c) sample FLI hot-pressed from foils. The sintered sample shows 12% residual microporosity in the Ti–6Al–4V matrix (M), while the two hot-pressed matrices are fully dense. No iron interdiffusion occurred, as the wires (W) were carbon rich and formed a continuous TiC layer at their surfaces.

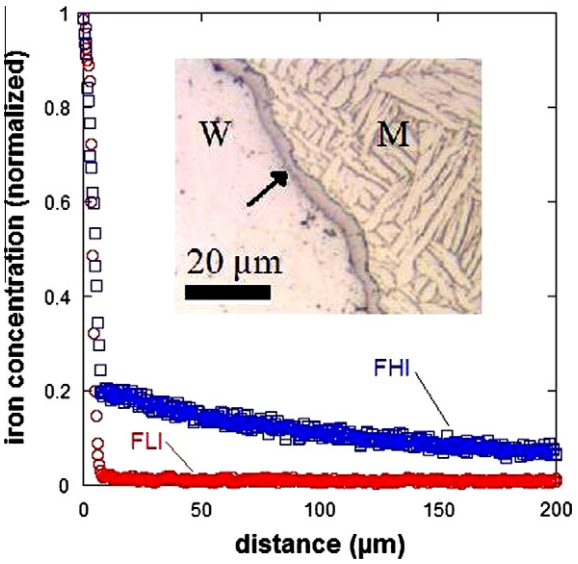

Fig. 2. EDX profiles of iron content along a radial direction from steel wire in hot-pressed foil samples FLI and FHI. The origin is at the wire/matrix interface and the Fe concentration is normalized to the maximum Fe concentration in the wire. Inset: SEM image of cross-section of sample FLI 2, showing steel wire (W) surrounded by densified Ti–6Al–4V matrix (M). A TiC layer (arrow) is present at the interface.

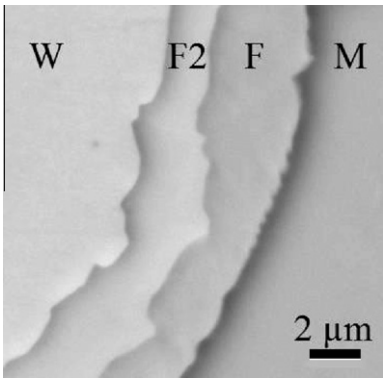

Fig. 3. SEM micrograph of cross-section of interface between low-carbon steel wire (W) and Ti–6Al–4V alloy matrix (M) showing two thin layers of intermetallics: $TiFe_2$ (F2) immediately adjacent to the steel wire and TiFe (F) adjacent to the matrix.

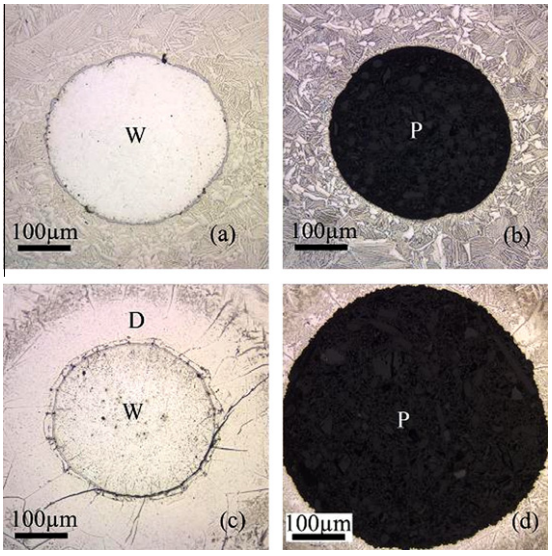

Fig. 4. Optical micrographs of etched cross-sections: (a) sample PLI with high-carbon steel wire (W) after hot pressing; (b) sample PLI after subsequent electrochemical steel removal with pore (P) in black replicating exactly the wire; (c) sample PHI with low-carbon steel wire (W) after hot pressing showing iron interdiffusion zone (D); and (d) sample PHI after subsequent electrochemical steel removal with pore (P) in black extending to most of the interdiffusion zone.

and a concomitant decrease in the diameter of the low-carbon steel wire from 356 to ~310 μm.

3.2. Wire dissolution

Fig. 5a and b show samples PLI and FHI 1 prior to mechanical testing after steel mesh removal. As shown in Figs. 5a and 4b, the PLI sample exhibits cylindrical pores, exactly replicating the original 356 μm diameter steel wires. Figs. 5b and 4d show that the PHI sample has pores extending to a diameter of ~530 μm, confirming that both the wire and the adjacent Fe-containing Ti–6Al–4V matrix

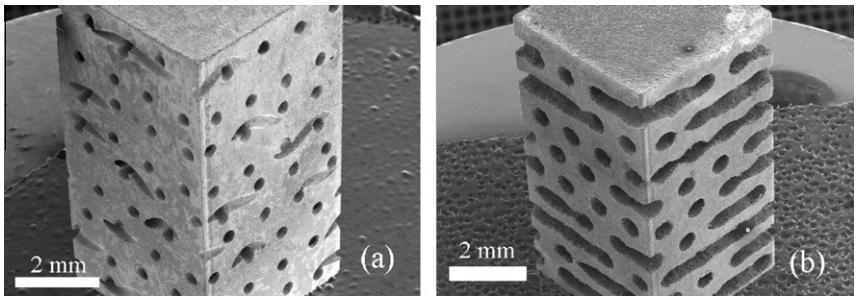

Fig. 5. SEM image of PLI (a) and FHI 1 (b) samples used for compressive testing.

were removed during dissolution. These micrographs illustrate that the amount of porosity can be tailored by allowing more or less interdiffusion by controlling the sintering time and/or temperature and the resulting width of the diffusion zone. However, if the overlap of diffusion regions from neighboring wires becomes too extensive, regions of very high porosity can form locally, weakening the material.

Complete removal of the carburized steel wires was completed in 18–21 h, as measured by a mass loss of 250 mg per sample (with dimensions of $4.5 \times 4.5 \times 9$ mm^3 and an initial mass of 910 mg). Complete removal of uncarburized steel wires and their associated interdiffusion regions, as measured by a mass loss of 480 mg, was achieved after 67–74 h (when negligible conversion current was measured). Average material removal rates for the PLI and FLI samples were 1.5–1.7 mm^3 h^{-1}, while those for PHI and FHI samples were 1.1–1.2 mm^3 h^{-1}. These rates compare favorably with those for laser machining [51] and electro-discharge machining (EDM) [52–55] of cylindrical holes with similar dimensions (Fig. 6). Because all wires are being removed simultaneously, the net removal rate increases linearly with the number of wires exposed to the electrolyte. However, the average removal rates decrease rapidly with the depth of the holes [38], because of the increase in diffusion distance for the electrolyte and the corrosion products. In Fig. 6, two points are given for the present steel wires electro-dissolution process, corresponding to one and three samples processed simultaneously. Increasing the number of samples, decreasing the hole depth or increasing their diameters would increase the average material removal rate. The rates reflect material removal only, not the production time associated with the powder process. By contrast, for methods that create holes sequentially (laser machining and EDM), these rates are insensitive to the number of holes created and, to a first extent, the depth of the holes (but increase with hole diameter).

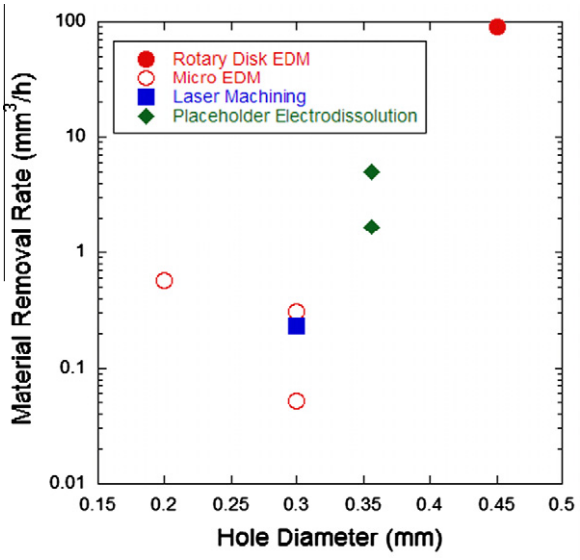

Fig. 6. Material removal rate for several titanium alloy processing methods: rotary disk EDM [52], microEDM [53–55], laser drilling [51] and the current method based on placeholder electro-dissolution (one and three samples with present dimensions).

Additional issues are the recast layer formed on the surface of the holes for EDM and laser drilling, and tool fragility for micromachining and microdrilling. Also, the geometry of the pores produced by these methods is limited to straight holes, slits and surface impressions, whereas electro-dissolution of embedded wires can create continuous pores with widely varying geometry and orientation, limited only by the original steel wires and their placement in the Ti–6Al–4V matrix. One possible issue with the current process using uncarburized wires is the remaining Fe in the matrix that is not removed electrochemically. Low levels of Fe in solid solution within Ti–6Al–4V may be deleterious to its corrosion resistance and/or biocompatibility. It is known, however, that iron additions up to 0.2 wt.% in Ti–6Al–4Vs increase the tensile strength and yield stress, and may thus be beneficial [56]. If further research indicates that Fe cannot be tolerated, even at low levels, within these porous Ti–6Al–4V materials, then only carburized steel wires preventing Fe diffusion can be used.

Oxygen analysis of the porous Ti–6Al–4V samples was performed by Wah Chang Analytical Laboratory and provided 0.17 wt.% for FLI 1 and FLI 2. The as-received foils were not analyzed for oxygen content, which was most probably low (e.g. ~0.07 wt.%) to maximize ductility for the foil rolling process. The oxygen contamination due to the densification process is thus on the order of 0.17–0.05 = 0.1 wt.%, which is much less than the oxygen values (1.2–1.8%) that detrimentally affected the ductility of the sintered samples in Ref. [39]. This is confirmed by

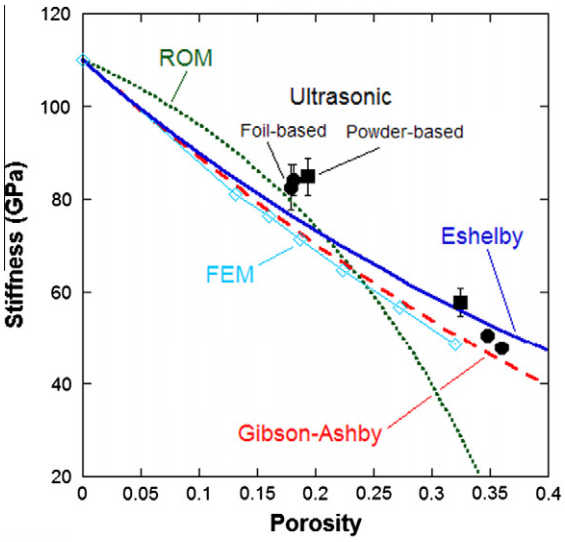

Fig. 7. Plot of stiffness vs. porosity as determined by ultrasonic testing and as calculated by the Eshelby model (Eq. (4)), Gibson–Ashby model (Eq. (5)), ROM model (Eq. (8)) and FEM simulation.

the high compressive ductility of the present porous Ti–6Al–4V, as described in the next section.

3.3. Stiffness

3.3.1. Experimental measurements

Fig. 7 plots the stiffness E_{33}, as determined ultrasonically in the longitudinal direction, as a function of the porosity of the Ti–6Al–4V specimens. Table 1 also lists the other two stiffness values, $E_{11}$and E_{22}, as well as the Young's modulus as measured from compressive stress–strain experiments in the longitudinal direction. These are somewhat lower (by ~5 GPa) than the ultrasonic measurements of E_{33} for the low-porosity samples. The discrepancy is however very large (~30 GPa) for high-porosity samples. This may be due to the small width of the walls separating the pores, which undergo microplastic deformation in the apparently linear regime of the stress–strain curve.

Predictions from four models are also plotted in Fig. 7: the first two models (Eshelby and Gibson–Ashby) are shown for qualitative comparison only, since they are derived for materials with equiaxed porosity and different pore connectivity (isolated pores and cylindrical struts, respectively). The other two models (rule-of-mixtures (ROM) and finite-element method (FEM)) take into account the elongated pore geometry and are thus useful for a quantitative comparison with our experimental data. Each of these four models is described in detail in the following sections.

3.3.2. Approximate models for equiaxed porosity

First, the Eshelby model considers a random distribution of isolated, spherical inclusions, assumed to be pores with zero stiffness. The composite (foam) compliance matrix S_c is given by [57]:

$$S_c = C_m^{-1} - (f((C_i - C_m)(S - f(S - I)) + C_m)^{-1}(C_m)^{-1}(C_i - C_m)) \quad (4)$$

where C_m is the Ti–6Al–4V elastic stiffness matrix (assumed to be isotropic and calculated assuming a Young's modulus of 110 GPa [58] and a Poisson's ratio of 0.22), f is the volume fraction of inclusion (equal to porosity p for a foam), C_i is the inclusion stiffness matrix (taken to be zero for pores), S is the Ti–6Al–4V elastic compliance matrix and I is the identity matrix.

Second, the Gibson–Ashby model is derived for cellular materials with uniform struts deforming by bending, expected to be valid for foams with relative densities of 0.03–0.3 [59] but found to fit experimental data to higher

Table 1
Porosity and longitudinal compressive engineering mechanical properties of all samples produced by hot pressing (PLI, FLI, PHI, FHI) and three comparable samples produced by sintering [39] with residual matrix porosity, with pore-free, cast Ti–6Al–4V [58,62] listed for comparison.

Sample	Process	Porosity (%)	Compressive measurements			Ultrasonic measurements	
			Yield strength (MPa)[a]	Peak strength (MPa)[a]	Stiffness (GPa)[b]	E_{33} (GPa)	E_{11}, E_{22} (GPa)
PLI	Hot-pressed	19.3	526	831	77.0	84.9	91.8
FLI 1		17.9	495	>947[c]	80.7	82.6	95.0
FLI 2		18.1	503	810	80.1	84.2	95.5
LI [39]	Sintered	20.7	267	432	39.9	–	–
PHI	Hot-pressed	32.4	209	341	21.9	57.9	78.3
FHI 1		36.1	216	>732[c]	19.7	47.9	72.1
FHI 2		34.8	190	>729[c]	20.7	50.7	68.0
II [39]	Sintered	34.0	265	513	14.8	–	–
HI [39]		41.4	176	341	4.8	–	–
Ti–6Al–4V [58,62]	Cast/mill-anneal	0	970	1680	105–116	–	–

The ultrasonically measured stiffnesses in the transverse (E_{11} and E_{22}) and longitudinal directions (E_{33}) of all samples were produced by hot pressing.
[a] Typical error: 10 MPa.
[b] Typical error: 1 GPa.
[c] Compression test stopped before reaching peak strength.

densities [60]. The Young's modulus E of the cellular material is given by [59]:

$$\frac{E}{E^*} = C\left(\frac{\rho}{\rho^*}\right)^2 \tag{5}$$

where E^* is the Young's modulus of the dense material, ρ and ρ^* are respectively the densities of the foam and dense material (with $p = 1 - \rho/\rho^*$), and the geometric constant, C, is unity. Surprisingly, as shown in Fig. 7, both the Eshelby and Gibson–Ashby predictions are relatively close to the experimental data for foams with $p \sim 0.19$ and $p \sim 0.34$, despite the widely different geometrical assumptions made for their derivations.

3.3.3. Simplified ROM model

For the ROM model, we assume that cylindrical pores can be modeled as rectangular slots of the same cross-sectional area. Fig. 8 shows the steps followed to derive this approximate model. Fig. 8a is a simplified model of the Ti–6Al–4V matrix after the steel mesh has been removed. The interweaving channels are replaced by straight, parallel, cylindrical holes in two stacked plates. Treating these separate layers as non-interacting, their longitudinal strains in the 3-direction can be combined into a ROM model. The volume fraction of the two porous layers is denoted as V_I and that of the solid as V_{II}, with $V_I + V_{II} = 1$.

We then approximate each of the two individual sublayers in the porous volume (with fraction V_1) as a solid layer with rectangular slots (Fig. 8b). The two sublayers are assumed to not interact, so, when longitudinally loaded along the 3-axis (Fig. 8b), they deflect elastically to the same strain e_I:

$$\varepsilon_I = \frac{\sigma/V_m}{E^*}, \tag{6}$$

where σ is the applied uniaxial stress and V_m is the matrix volume fraction in the sublayers. Overall, the composite (foam) strain in the 3-direction, e_{tot}, is the weighted sum of the strains of the two regions:

$$\varepsilon_{tot} = V_I \cdot \varepsilon_I + V_{II} \cdot \varepsilon_{II} = \frac{V_I \cdot \sigma/V_m}{E^*} + \frac{V_{II} \cdot \sigma}{E^*} = \frac{\sigma}{E^*}\left(\frac{V_I}{V_m} + (1 - V_I)\right) \tag{7}$$

Thus, the composite (foam) longitudinal Young's modulus is:

$$E_{foam} = \frac{\sigma}{\varepsilon_{tot}} = E^* \cdot \left[1 + V_I\left(\frac{1}{V_m} - 1\right)\right]^{-1} \tag{8}$$

where the parameters V_m and V_I are connected by geometry to the overall porosity p as:

$$p = (1 - V_m) \cdot V_I \tag{9}$$

An additional equation is needed to eliminate V_m and V_I from Eq. (8). The fraction of open area of the mesh is given by the supplier as 44.2%, which is equal to the fraction of matrix in the porous sublayer for exactly replicated pores with carburized steel. Thus, for the PLI and FLI samples, $V_m = 0.442$ and $p = 0.19$, and Eq. (9) gives $V_I = 0.341$.

For the PHI and FHI samples with uncarburized wires and $p = 0.34$, the value of V_m can be estimated as follows. The pores, with original diameter $d_1 = 356$ μm, have increased their diameter to d_2=528 μm diameter. Estimating, from cross-sections, that a factor $k = 0.25$ (25%) of the diffusion areas overlap between neighboring wires, the effective area (and thus volume) increase is given as $(1 - k)(d_2/d_1)^2 = 1.65$ for the present case. The pore fraction $(1 - V_m)$ is then increased by this same factor from 0.558 to 0.921, so $V_m = 0.079$. Then Eq. (9) with the measured value $p = 0.34$ gives $V_I = 0.369$.

Using these two end-points values ($V_I = 0.369$, $p = 0.34$ and $V_I = 0.341$, $p = 0.19$), we use a linear interpolation of V_I with respect to the overall porosity p:

$$V_I = \frac{p - 0.19}{0.34 - 0.19}(0.369 - 0.341) + 0.341 \tag{10}$$

Introducing Eqs. (9) and (10) into Eq. (8), E_{foam} can then be calculated with only two parameters: the overall porosity, p, and the Young's modulus of Ti–6Al–4V, E^*. The results of this ROM model are plotted alongside ultrasonic data and other model predictions in Fig. 7. Despite the many simplifications of this model, its prediction for the Young's modulus is surprisingly close to the experimental data for $p = 0.19$ but strongly underestimates the data for $p = 0.34$, possibly because the parameter $k = 0.25$ is underestimated.

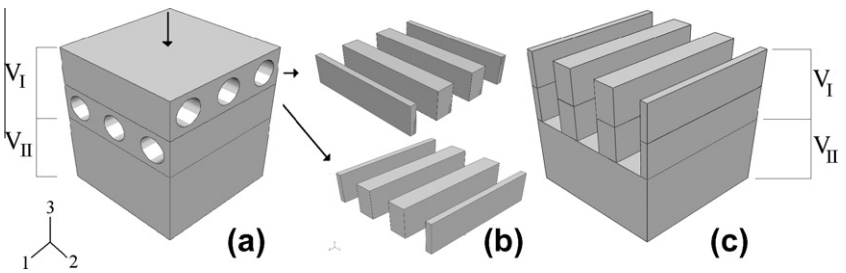

Fig. 8. ROM model as used to calculate stiffness. (a) A simplified geometry with a first region (volume fraction V_I) consisting of two orthogonal sublayers each with parallel cylindrical holes and a second pore-free region (volume fraction V_{II}). (b) Simplification of cylindrical holes into rectangular slots with same volume fraction. (c) ROM model with slotted sublayers stacked parallel to each other.

3.3.4. Finite-element model

Finally, the FEM is used to model porous Ti–6Al–4V with a representative volume element (RVE), shown in Fig. 9, with the following boundary conditions. A rigid horizontal plate constrains translation of the bottom face of the RVE, two mirror planes constrain translation and rotation of two adjacent side (vertical) faces, two linear constraints on the other two adjacent side (vertical) faces allow translation as the element compresses while still remaining vertical, and one linear constraint on the top face maintains its horizontal orientation while allowing vertical displacement in the 3-direction upon compression. These periodic boundary conditions simulate an infinite body, with the RVE being replicated in the 1- and 2-directions by mirror planes.

The RVE dimensions in the 1–2 plane were $1.068 \times 1.068\ mm^2$ (corresponding to the experimental wire center-to-center spacing of the steel mesh) and the RVE height in the 3-direction was 1.325 mm. The pore geometry was simplified by considering two straight (rather than wavy) cylindrical channels, interwoven with two wavy channels (Fig. 9). The pore diameter was 356 μm (PLI and FLI, $p = 19\%$) or 528 μm (PHI and FHI, $p = 32\%$), based on experimental measurements. Four additional pore diameters were considered, to create a total of six RVEs. All calculations were performed with the commercial software ABAQUS (v. 6.7–3, Simulia).

Fig. 7 shows stiffness values from the FEM simulations for the six RVEs with porosity between $p = 13\%$ and $p = 32\%$. The stiffness was calculated from a stress vs. strain simulation (between 0 and 100 MPa) in the elastic portion of the calculated stress–strain curve. The agreement with the Gibson–Ashby model (Eq. (5)) is serendipitous, given how radically different the two models are. All experimental data are 2–10 GPa above the FEM values, possibly because the two straight pores in the simulation decrease stiffness more than the wavy pores in the samples and because the overlap volume of the diffusion areas between neighboring wires is oversimplified. A better representation will have to await tomographic imaging of the samples, which is beyond the scope of the present paper.

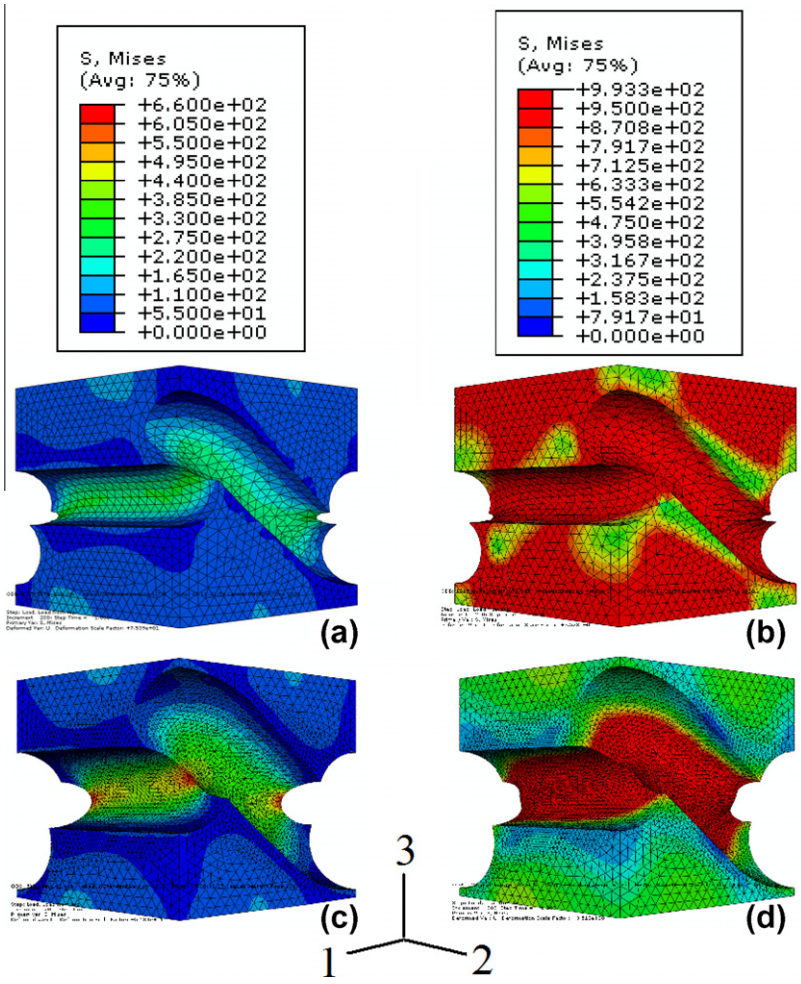

Fig. 9. FEM models with (a and b) 19% porosity and (c and d) 32% porosity. Von Mises stress distribution is shown (a and c) for an applied uniaxial compressive stress of 100 MPa and (b and d) for an applied uniaxial strain of 3%, corresponding to an applied stress of (b) 671 MPa and (d) 383 MPa. In (a and c) the yield stress is not exceeded anywhere in the model, while in (b and d) red areas denote stresses above the yield strength of 950 MPa. (For interpretation of the references to color in this figure legend, the reader is referred to the web version of this article.)

Simulations were also run on stacks of two RVEs with varying wire orientations for models with $p = 32.0\%$ and 18.7%. These variations are denoted as parallel (Fig. 10a), inverted (Fig. 10b) and rotated (Fig. 10c). As compared to the baseline single-cell RVE stiffness values of 48.6 GPa ($p = 32.0\%$) and 71.3 GPa ($p = 18.7\%$), the two-cell RVE result in very small stiffness variations of ±0.4 GPa, indicating that 90° or 180° rotations of the meshes and resulting pores have negligible effects on the longitudinal stiffness.

3.4. Plastic deformation

Fig. 11 shows the experimental stress–strain curves of the two series of Ti–6Al–4V materials with low porosity (PLI and FLI, $p \sim 19\%$) and high porosity (PHI and FHI, $p \sim 34\%$). All curves exhibit ductile behavior with plastic strains without failure exceeding 15% and all samples fail by shear after extensive collapse of individual pore layers, visible as serrations on the stress–strain curves and a steadily increasing stress due to densification. Mechanical properties are summarized in Table 1 and compared to sintered samples from Ref. [39] with similar overall porosity. These are weaker, less ductile and less energy absorbing, as expected from their matrix microporosity and much higher oxygen content (~1.2–1.8 wt.%).

Elasto-plastic FEM simulations were run to calculate the stress–strain curves of the two porous Ti–6Al–4V samples with $p = 19\%$ and 32%, using as input the stress–strain curve of dense Ti–6Al–4V with matrix yield strength of 950 MPa and strain hardening shown in Fig. 12, from Ref. [61]. The calculated curve for Ti–6Al–4V with the lowest porosity agrees reasonably well with the experimental one, but calculations overestimate the strength of the higher-porosity foam (Fig. 12). This may be due to sharp stress concentrations which are sensitively dependent on the details of the pore spatial arrangement and local overlap, which are not captured in the simplified RVE used here. These stress concentrations are visible in Fig. 9, which shows the two porosity levels at the same macroscopic strain (3%) corresponding to different applied stress, or the same applied stress (100 MPa) corresponding to different strains. Stress concentration leads to local yielding in the center of the RVE (Fig. 9c), with the plastic zone spreading to the rest of the RVE at higher stress, as illustrated by the red areas in Fig. 9b and d.

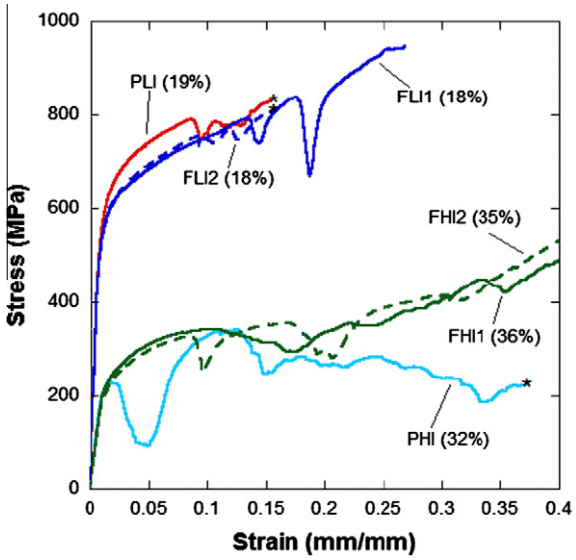

Fig. 11. Stress–strain curve for samples with low porosity (PLI and FLI) and high porosity (PHI and FHI). Duplicating experiments are noted with 1 and 2, and illustrate sample-to-sample repeatability. Asterisks denote catastrophic failure for PLI, FLI 2 and PHI. Numbers inside parentheses denote measured porosity.

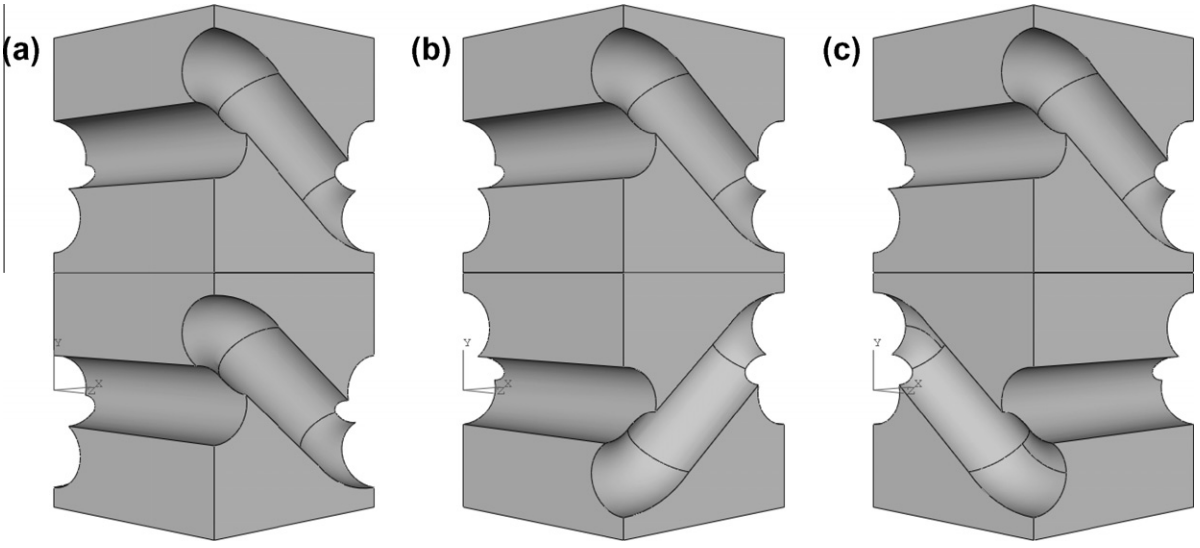

Fig. 10. FEM models consisting of two stacked cells for 18.7% porosity: (a) parallel stack with wires repeating vertically; (b) inverted stack with waved wires alternating in the vertical direction; and (c) rotated stack with straight wires positioned directly beneath waved wires.

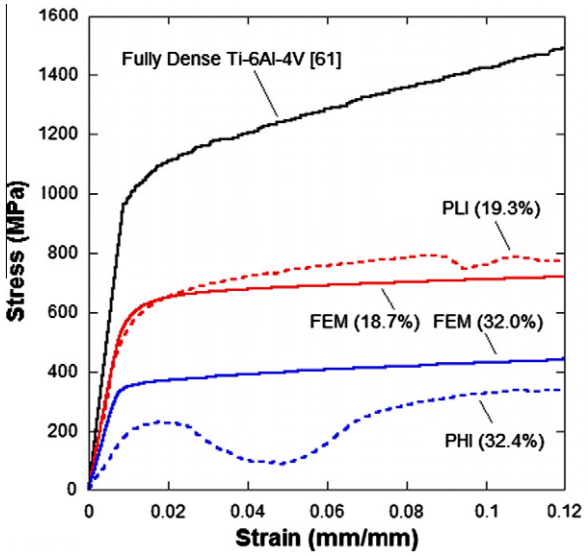

Fig. 12. Stress–strain curves for PLI and FLI samples as determined by FEM simulation and as measured by mechanical testing. The low-porosity sample matches better with simulation than the high-porosity sample. The dip near 4% strain for PHI is due to the collapse of a pore layer.

4. Conclusions

A network of elongated pores is created in Ti–6Al–4V by a two-step replication process. First, a composite is created by densifying a preform consisting of steel fiber meshes and Ti–6Al–4V powders or foils, relying on transformation superplasticity. Second, the steel wires are removed electrochemically to produce porosity in the Ti–6Al–4V matrix. This method offers wide freedom for altering the amount, shape, size, orientation, tortuosity and interconnectivity of the pores, which can all be manipulated through the steel wire geometry. Also, the pore diameter can be increased by creation of a Fe-containing diffusion zone during densification that is subsequently dissolved together with the steel wires. Ti–6Al–4V samples are manufactured by this method with 19% and 34% open porosity (without and with creation and dissolution of Fe-containing zones, respectively), replicating stacks of meshes of 356 μm diameter steel wires. The stiffness of these porous samples is in reasonable agreement with various models for foams with equiaxed and elongated pores. Finite-element models developed to predict their plastic compressive behavior illustrate local stress concentrations present at regions where pores overlap.

Acknowledgements

This research was supported by the National Science Foundation (NSF) through Grant DMR-0505772. D.J.J. was also supported by an NSF Graduate Research Fellowship. The authors acknowledge the assistance of the following Northwestern University members: Ms. K. Pappacena (ultrasonic measurements), Dr. B. Ye (powder densification and FEM) and Mr. F. Yuan (FEM).

References

[1] Geetha M, Singh A, Asokamani R, Gogia A. Prog Mater Sci 2008.
[2] van Lenthe GH, Willems MMM, Verdonschot N, Malefijt MCD, Huiskes R. Acta Orthop Scand 2002;73:630.
[3] Verdonschot N, Huiskes R. J Appl Biomater 1994;5:235.
[4] Kujala S, Ryhanen J, Danilov A, Tuukkanen J. Biomaterials 2003;24:4691.
[5] Dunand DC. Adv Eng Mater 2004;6:369.
[6] Itin VI, Ponter VE, Khodorenko VN, Chobanyan ML, Mirgazizov MZ, Korosteleva EN, et al. Powder Metall Metal Ceram 1997;36:479.
[7] Thieme M, Wieters KP, Bergner F, Scharnweber D, Worch H, Ndop J, et al. J Mater Sci – Mater Med 2001;12:225.
[8] Zou CM, Zhang E, Li MW, Zeng SY. J Mater Sci – Mater Med 2008;19:401.
[9] Sypeck DJ, Parrish PA, Wadley HNG. In: Schwartz DS, Shih DS, Wadley HNG, Evans AG, editors. Porous and cellular materials for structural applications. Pittsburgh (PA): MRS; 1998. p. 205.
[10] Queheillalt DT, Choi BW, Schwartz DS, Wadley HNG. Metall Mater Trans A – Phys Metall Mater Sci 2000;31:261.
[11] Spoerke ED, Murray NGD, Li H, Brinson LC, Dunand DC, Stupp SI. J Biomed Mater Res, Part A 2008;84A:402.
[12] Murray NGD, Dunand DC. Acta Mater 2004;52:2269.
[13] Murray NGD, Dunand DC. Compos Sci Technol 2003;63:2311.
[14] Jee CSY, Ozguven N, Guo ZX, Evans JRG. Metall Mater Trans B – Process Metall Mater Process Sci 2000;31:1345.
[15] Bram M, Stiller C, Buchkremer HP, Stover D, Baur H. Adv Eng Mater 2000;2:196.
[16] Wen CE, Mabuchi M, Yamada Y, Shimojima K, Chino Y, Asahina T. Scripta Mater 2001;45:1147.
[17] Laptev A, Bram M, Buchkremer HP, Stover D. Powder Metall 2004;47:85.
[18] Dewidar MM, Lim JK. J Alloys Compd 2008;454:442.
[19] Tolochko NK, Savich VV, Laoui T, Froyen L, Onofrio G, Signorelli E, et al. Proc Inst Mech Eng Part L – J Mater-Des Appl 2002;216:267.
[20] Wu XH, Jing LA, Mel JF, Mitchell C, Goodwin PS, Voice W. Mater Des 2004;25:137.
[21] Hayashi T, Maekawa K, Tamura M, Hanyu K. Jsme Int J Ser A – Solid Mech Mater Eng 2005;48:369.
[22] Hollander DA, von Walter M, Wirtz T, Sellei R, Schmidt-Rohlfing B, Paar O, et al. Biomaterials 2006;27:955.
[23] Heinl P, Muller L, Korner C, Singer RF, Muller FA. Acta Biomater 2008;4:1536.
[24] Okazaki K, Lee WH, Kim DK, Kopczyk RA. J Biomed Mater Res 1991;25:1417.
[25] Lee WH, Puleo DA. J Mater Sci Lett 1999;18:817.
[26] An YB, Oh NH, Chun YW, Kim DK, Park JS, Choi KO, et al. Surf Coat Technol 2006;200:4300.
[27] Jo YJ, Lee CM, Jang HS, Lee NS, Suk JH, Lee WH. J Mater Process Technol 2007;194:121.
[28] Li Y, Guo ZM, Hao JJ, Ren SB. Rare Metals 2008;27:282.
[29] Erk KA, Dunand DC, Shull KR. Acta Mater 2008;56:5147.
[30] Li X, Wang C, Zhang W, Li Y. Mater Lett 2008;2:1.
[31] Gaytan SM, Murr LE, Medina F, Martinez E, Lopez MI, Wicker RB. Mater Technol 2009;24:180.
[32] Lee MH, Kim KB, Han JH, Eckert J, Sordelet DJ. J Phys D – Appl Phys 2008;41.
[33] Chino Y, Dunand DC. Adv Eng Mater 2009;11:52.
[34] Chino Y, Dunand DC. Acta Mater 2008;56:105.
[35] Fife JL, Dunand DC, Voorhees PW. J Mater Res 2008;24:117.
[36] Barr SA, Luijten E. Acta Mater 2010;58:709.
[37] Yook SW, Yoon BH, Kim HE, Koh YH, Kim YS. Mater Lett 2008;62:4506.

[38] Kwok PJ, Oppenheimer SM, Dunand DC. Adv Eng Mater 2008;10:820.
[39] Jorgensen DJ, Dunand DC. Mater Sci Eng, A 2010;527:849.
[40] Momono T, Enjo T, Ikeuchi K. ISIJ Int 1990;30:978.
[41] Schuh C, Dunand DC. Int J Plast 2001;17:317.
[42] Schuh C, Dunand DC. Acta Mater 2001;49:199.
[43] Schuh C, Noel P, Dunand DC. Acta Mater 2000;48:1639.
[44] Schuh CA, Dunand DC. Acta Mater 2002;50:1349.
[45] Ye B, Matsen MR, Dunand DC. Acta Mater 2010;58:3851.
[46] Musgrave MJP. Crystal acoustics; introduction to the study of elastic waves and vibrations in crystals. San Francisco (CA): Holden-Day; 1970.
[47] Ledbetter HM, Read DT. J Appl Phys 1977;48:1874.
[48] Wilkes TE, Young ML, Sepulveda RE, Dunand DC, Faber KT. Scripta Mater 2006;55:1083.
[49] Ledbetter HM, Labrecque JF, Dahnke JL. Phys Status Solidi A – Appl Res 1981;67:643.
[50] Brama M, Rhodes N, Hunt J, Ricci A, Teghil R, Migliaccio S, et al. Biomaterials 2007;28:595.
[51] Lash JS, Gilgenbach RM. Rev Sci Instrum 1993;64:3308.
[52] Chow HM, Yan BH, Huang FY. J Mater Process Technol 1999;91:161.
[53] Pradhan BB, Bhattacharyya B. Proc Inst Mech Eng Part B – J Eng Manuf 2008;222:163.
[54] Lin YC, Chow HM, Yan BH, Tzeng HJ. Int J Adv Manuf Technol 2007;33:489.
[55] Zhao WS, Wang ZL, Di SC, Chi GX, Wei HY. J Mater Process Technol 2002;120:101.
[56] Simbi DJ, Scully JC. Mater Lett 1996;26:35.
[57] Clyne TW, Withers PJ. An introduction to metal matrix composites. Cambridge: Cambridge University Press; 1993.
[58] Welsch G, Boyer R, Collings EW. Materials properties handbook: titanium alloys. Materials Park (OH): ASM International; 1994.
[59] Gibson LJ. Annu Rev Mater Sci 2000;30:191.
[60] Murray NGD, Dunand DC. J Mater Res 2006;21:1175.
[61] Sarsfield H, Wang L, Petrinic N. J Mater Sci 2007;42:5085.
[62] Li QZ, Chen EY, Bice DR, Dunand DC. Metall Mater Trans A – Phys Metall Mater Sci 2008;39A:441.